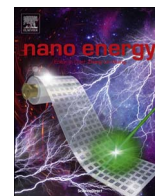




ELSEVIER

Contents lists available at ScienceDirect

Nano Energy

journal homepage: www.elsevier.com/locate/nanoen

Novel exciton dissociation behavior in tin-lead organohalide perovskites

Guoming Lin^{a,e,1}, Yuanwei Lin^{b,c,1}, Huan Huang^a, Rongli Cui^a, Xihong Guo^a, Bing Liu^a, Jinqun Dong^a, Xuefeng Guo^{b,d,*}, Baoyun Sun^{a,*}

^a Institute of High Energy Physics, Chinese Academy of Sciences (CAS), Beijing 100049, China

^b Beijing National Laboratory for Molecular Sciences (BNLMS), State Key Laboratory for Structural Chemistry of Unstable and Stable Species, College of Chemistry and Molecular Engineering, Peking University, Beijing 100871, China

^c Center for Nanoscience and Nanotechnology, Academy for Advanced Interdisciplinary Studies, Peking University, Beijing 100871, China

^d Department of Advanced Materials and Nanotechnology, College of Engineering, Peking University, Beijing 100871, China

^e Fujian Institute of Research on the Structure of Matter, Chinese Academy of Sciences (CAS), Fuzhou, Fujian 350002, China

ARTICLE INFO

Article history:

Received 20 March 2016

Received in revised form

31 July 2016

Accepted 6 August 2016

Available online 6 August 2016

Keywords:

Tin-lead organohalide perovskites

Fullerenes

Solar cells

Exciton dissociation behaviors

ABSTRACT

The design of organic-inorganic trihalide perovskite solar cells with higher performance, lower environmental pollution, lower cost and easier of fabrication should be a significant stride towards their practical application. Nevertheless, the contribution of exciton dissociation behavior of the perovskite to this strategy has not been recognized comparing with film morphology, device architecture and fabrication process. Here we demonstrated a series of solution-processed solid-state tin-lead organohalide perovskite photovoltaic solar cells using carefully selected fullerene derivatives as the electron transport layer. The hybrid excitonic feature of $\text{CH}_3\text{NH}_3\text{Sn}_{0.5}\text{Pb}_{0.5}\text{I}_3$ was revealed for the first time by comparing the exciton dissociation behaviors of $\text{CH}_3\text{NH}_3\text{Sn}_{0.5}\text{Pb}_{0.5}\text{I}_3$ with conventional excitonic semiconductor in both planar heterojunction solar cells and lateral architecture photosensors. By optimizing the lowest unoccupied molecular orbital level of electron transport layer materials, high open circuit voltage of 0.69 V, short circuit photocurrent density of 22.8 mA cm^{-2} and power conversion efficiency of more than 10% were achieved with the incident photon conversion efficiency spectra onset reaching 1050 nm. These devices may work as high performance photodetectors with a broad spectral response expanding from UV-visible to near-infrared. Our results have suggested the exciton dissociation behavior to be an efficient perspective for the improvement of perovskite solar cells.

© 2016 Elsevier Ltd. All rights reserved.

1. Introduction

The emergence of organohalide perovskites (AMX_3 , $\text{A} = \text{CH}_3\text{NH}_3$ (MA^+), $\text{NH}_2\text{CH}=\text{NH}_2^+$, $\text{M} = \text{Pb}$, Sn , Ge , $\text{X} = \text{Cl}$, Br , I) as light harvesters has revolutionized the photovoltaic technologies and underwent fast development in recent years [1–3]. More recently, it was observed that perovskite materials with high optical absorption coefficients, long photoexcited carrier lifetimes, and long diffusion lengths played a critical roles for high photovoltaic performance [4,5]. Photovoltaic devices based on lead organohalide perovskites materials with TiO_2 as the electron transport layer (ETL) material and 2,2',7,7'-tetrakis-(N,N-di-p-meth-

* Corresponding author at: College of Chemistry and Molecular Engineering, Peking University, Beijing 100871, China.

** Corresponding author at: Institute of High Energy Physics, Chinese Academy of Sciences (CAS), Beijing 100049, China

E-mail addresses: guoxf@pku.edu.cn (X. Guo), sunby@ihep.ac.cn (B. Sun).

¹ These authors contributed equally to this work.

oxyphenylamine)-9,9-spirobifluorene (spiroOMeTAD) as the hole transport layer (HTL) material have been reported to deliver high power conversion efficiency (PCE) even above 20% [6–9].

However, the environmental toxicity of lead may limit commercial applications of lead organohalide perovskite (LOP) solar cells [3]. Finding ways to create lead-free perovskites without sacrificing device performance is especially critical for perovskite photovoltaics. Partial or full replacement of lead with non-toxic tin is a viable alternative. Several groups have reported a broader absorption edge for tin-lead organohalide perovskite (TLOP) (reaching 1060 nm) than the LOP (less than 800 nm) [10–12]. In theory, light harvesting in the near-infrared (NIR) region is required to achieve higher PCE [11]. Unfortunately, recently reported TLOP solar cells with absorption onset more than 1000 nm displayed much lower PCEs as LOP solar cells [10–12]. Besides, all these reports employed complex mesoporous TiO_2 structures that require a high temperature (above 450 °C) sintering process. Further development of perovskite solar cells is limited by these extreme processing conditions, especially on flexible substrates. To

improve the performance of tin-lead organohalide perovskite solar cells a low temperature solution process with low cost and ease of fabrication would be required. For this purpose, planar heterojunction photovoltaic devices with poly(3,4-ethylenedioxythiophene): poly(styrenesulfonate) (PEDOT: PSS) as HTL materials and functionalized fullerenes as ETL materials could be considered. Although recent works have shown differences between LOPs and conventional excitonic materials, such as organic semiconductors [13], the exciton dissociation behavior of TLOPs has not been reported yet. However, both for fundamental understanding and practical applications it is quite necessary to reveal the exciton features in these tin-lead organohalide perovskites.

In the Frenkel exciton based planar heterojunction solar cells, the energy level of light absorbing materials and the ETL materials should be carefully selected. Fullerene derivatives are one of the most commonly used ETL materials for photovoltaic devices because of their high intrinsic electron affinity, low-lying lowest unoccupied molecular orbital (LUMO) energy levels, fast photo-induced electron-transfer and good availability [14,15]. The intrinsic properties of fullerene molecules, such as optical properties, frontier orbitals and intermolecular interaction can be customized by the functionalization of these buckyballs [16,17]. The LUMO levels of fullerene can be modulated by altering the number of adduct groups, which has been an effective strategy to achieve higher V_{OC} values of the devices [18,19]. Moreover, incorporation of an n-type functional fullerene interlayer between the electron transport and the inorganic layer can minimize the exciton recombination losses at the interface and improve charge transfer from the ETL to the electrodes, leading to the improvement of device performance [20].

Herein, three novel fullerene derivatives with different adduct numbers and discrete LUMO levels were synthesized. A series of solution-processed solid-state photovoltaic devices using PEDOT: PSS as HTL and functionalized fullerenes as ETL materials were fabricated and characterized by optimizing the preparation of the TLOP layer and carefully choosing other materials. For $MASn_{0.5}Pb_{0.5}I_3$ based photovoltaic solar cells (PSCs), the V_{OC} output is found to be dependent on the LUMO energy level of the ETL materials (fullerene or fullerene derivatives). With the optimized LUMO level of ETL materials, the $MASn_{0.5}Pb_{0.5}I_3$ PHJ solar cells show high open circuit voltage of 0.69 V, short circuit photocurrent density of 22.8 mA cm^{-2} , high PCE of more than 10% and photodetection performance with spectral response from UV-visible to near-infrared ($\sim 1050 \text{ nm}$). Due to the high performance of both vertical and lateral architecture devices, the exciton feature of $MASn_{0.5}Pb_{0.5}I_3$ perovskite should be a novel Frenkel-Wannier-Mott exciton hybridization. Our results have significant impact on the achievement of high performance and low pollution tin-lead organohalide perovskite solar cells through the low temperature solution process.

2. Results and discussion

2.1. Synthesis and characterization of tin-lead organohalide perovskites and fullerene derivatives

The synthetic details of perovskite materials are described in Experimental. As shown in Fig. 1a, the absorption spectrum of $MASn_{0.5}Pb_{0.5}I_3$ thin film covers the entire UV-visible and near-infrared spectra with an onset at 1060 nm. Fig. 1b presents the X-ray diffraction (XRD) patterns obtained from the $MASn_{0.5}Pb_{0.5}I_3$ thin film on silicon wafers. The formed tetragonal structure matches that of more widely used perovskite $CH_3NH_3PbI_3$ ($MAPbI_3$), showing that in this case, changing the central metal atom does not severely affect the overall crystal structure of the material. The

quantitative EDX analysis shows a Sn: Pb atomic ratio around 49:51 in the $MASn_{0.5}Pb_{0.5}I_3$ film, which is quite close to the nominal 50:50 ratio given by stoichiometry of the precursor solutions (Fig. 1c). With appropriate solvent engineering techniques, $MASn_{0.5}Pb_{0.5}I_3$ films on the ITO/PEDOT: PSS substrate can be made extremely uniform. Scanning electron microscopy (SEM) displays the surface morphology of the fabricated $MASn_{0.5}Pb_{0.5}I_3$ film on top of the ITO/PEDOT: PSS layer (Fig. 1d). The film surface is composed of well-developed grains with sizes of a few hundred nanometers covering the entire surface of the PEDOT: PSS layer perfectly. Atomic force microscopy (AFM) measurements shows that the 290 nm-thick film is very smooth with a RMS (root mean square) roughness of 10.8 nm in an area of $10 \mu\text{m} \times 10 \mu\text{m}$ (Fig. 1e, f and Fig. S1). The quality of the perovskite film is highly critical in affecting the performance of solar cells [21,22]. The perovskite layer formed in this work is rather smooth when compared with the reported before.

For the ETL materials, Fig. 1g presents the chemical structures of three commercially available fullerene or fullerene derivatives (C_{60} , PCBM and ICBA) and three novel fullerene derivatives (BPB-M, BPB-B and BPB-T, which had different adduct numbers of functional groups) with high solubility in organic solvents, such as chlorobenzene (CB) or *o*-dichlorobenzene (*o*-DCB). The synthesis and characterization details of the novel fullerene derivatives can be found in the Supplementary material. The material properties were further investigated by cyclic voltammetry (CV) and UV-Vis spectrophotometry. The CV spectra of these ETL materials are shown in Fig. 1h. The first half-wave reduction potentials (E_1) for BPB-M showed positive shifts of about 60 mV compared with that of $PC_{61}BM$. The LUMO levels of BPB-M, BPB-B and BPB-T were estimated from the empirical equation $LUMO \text{ level} = -(E_{red1} / 2 + 4.8)$ [16,24] are -3.74 eV , -3.61 eV and -3.48 eV , respectively. The LUMO energy levels of these ETL materials increase in the order of C_{60} , BPB-M, PCBM, BPB-B, BPB-T and ICBA. The absorption spectra of these ETL materials are shown in Fig. 1i, and the optical bandgaps (estimated from the absorption edges in toluene) are (1.85 eV, 1.70 eV, 1.77 eV) for BPB-M, BPB-B and BPB-T, respectively (Fig. 1i inset and Table 1).

2.2. Fabrication and characterization of $MASn_{0.5}Pb_{0.5}I_3$ /fullerenes Planar Heterojunction solar cells

For solar cell fabrication quality of perovskite film (such as coverage, RMS and crystallinity) critically influence device performance. Thus, for perovskite/fullerene PHJ solar cell fabrication, we choose $MASn_{0.5}Pb_{0.5}I_3$, to fabricate perovskite/fullerene PSCs, because it provides the smoothest thin film (See Fig. S1). Subsequently, a thin ($\sim 65 \text{ nm}$ thick) fullerene layer was deposited on the perovskite surface as ETL material. Using solvent processing made the surface become even more smooth (See Fig. S2). On the fullerene layer, 0.5 nm LiF as exciton- or hole-blocking layer and 100 nm Ag layer as a top electrode were deposited by vacuum evaporation. The schematic of the $MASn_{0.5}Pb_{0.5}I_3$ /fullerene PHJ solar cell is shown in Fig. 2a. The structure is further confirmed by the cross-sectional SEM image (Fig. S12). The energy levels of the device configurations are illustrated in Fig. 2b. The LUMO levels of BPB-B, BPB-T and ICBA are higher than that of $MASn_{0.5}Pb_{0.5}I_3$, while C_{60} , BPB-M and PCBM show lower LUMO levels than $MASn_{0.5}Pb_{0.5}I_3$. Fig. 2c shows photocurrent density-voltage (J - V) curves for these devices under simulated AM 1.5 illumination (100 mW/cm^{-2}). Fig. 2d shows the incident photon conversion efficiency (IPCE) spectra for these devices. The integral curves for IPCE are shown in Fig. S13. The shapes of the IPCE between 300 and 500 nm mainly originate from the transmittance spectrum of ITO/PEDOT: PSS. The IPCE range of the devices based on $MASn_{0.5}Pb_{0.5}I_3$ extends from 300 nm to 1050 nm, which is much

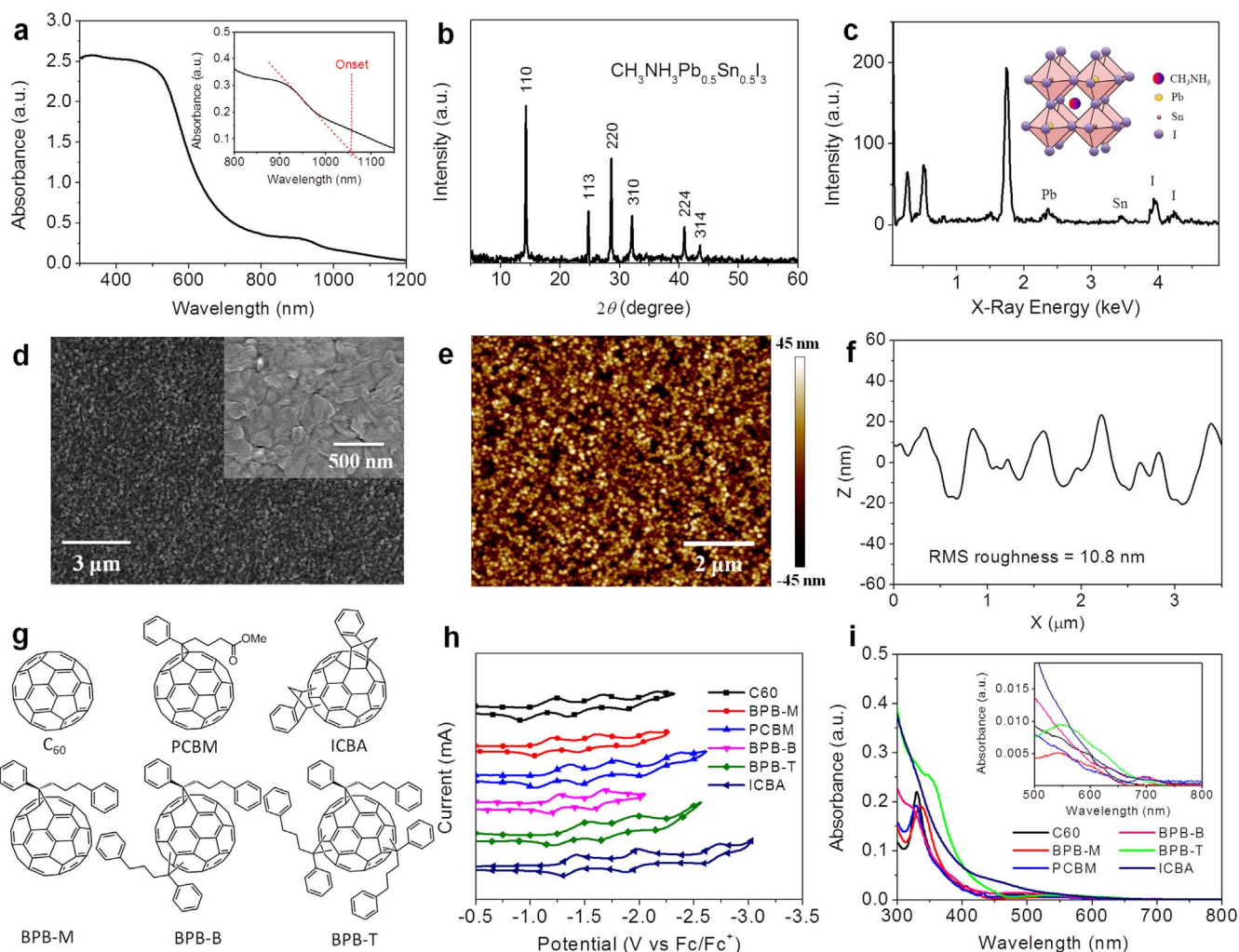


Fig. 1. Characterization of tin-lead organohalide perovskite and fullerene derivatives. (a) UV-Vis spectrum of $\text{MASn}_{0.5}\text{Pb}_{0.5}\text{I}_3$ perovskite thin film. Inset shows the onset of the absorbance. (b) XRD characterization of $\text{MASn}_{0.5}\text{Pb}_{0.5}\text{I}_3$ perovskite thin film. (c) EDX spectrum of $\text{MASn}_{0.5}\text{Pb}_{0.5}\text{I}_3$ perovskite thin film. The strongest peak is attributed to the silicon element in the substrate. Inset shows the scheme of $\text{MASn}_{0.5}\text{Pb}_{0.5}\text{I}_3$ crystal structure. (d) SEM images present the surface morphology of $\text{MASn}_{0.5}\text{Pb}_{0.5}\text{I}_3$ perovskite thin films. (e) AFM image of $\text{MASn}_{0.5}\text{Pb}_{0.5}\text{I}_3$ perovskite thin film. (f) The AFM characterization of $\text{MASn}_{0.5}\text{Pb}_{0.5}\text{I}_3$ perovskite. (g) Chemical structures of the electron transport materials (C_{60} and fullerene derivatives). (h) Cyclic voltammograms of the ETL materials. (i) UV-vis spectra of the ETL materials; inset shows the enlarged view of the onset.

broader than that of the devices based on MAPbI_3 (300–780 nm) [21,22,25]. The measured J_{SC} of the best device based on BPB-M (22.84 mA cm^{-2}) approximately agreed with the J_{SC} (22.76 mA cm^{-2}) calculated from the integration of IPCE (See Fig. S13). Open circuit voltage (V_{OC}) of 690 mV and a fill factor (FF) of 0.65, corresponding to a PCE of 10.24% has been obtained for $\text{MASn}_{0.5}\text{Pb}_{0.5}\text{I}_3$ device based on BPB-M, which is much higher than the PCE for the previously reported TiO_2 -based devices [10,11].

The performance of $\text{MASn}_{0.5}\text{Pb}_{0.5}\text{I}_3$ perovskite PHJ solar cells was quite sensitive to the variation of the LUMO of fullerenes. As LUMO level of fullerenes increases from -3.78 (C_{60}) to -3.47 eV (ICBA), the performance of the devices such as V_{OC} , J_{SC} , FF and PCE rapidly increase and then gradually fall. These photovoltaic parameters are summarized in Fig. 3. Recently, Wang *et al* demonstrated that discontinuities in the perovskite films would result in direct contact of fullerenes with PEDOT: PSS, and the Schottky junction formed between the different fullerenes and PEDOT: PSS would lead to the performance variation of the devices with different fullerene [26]. However, in our study, the solvent engineering technique was used to provide high quality $\text{MASn}_{0.5}\text{Pb}_{0.5}\text{I}_3$ perovskite films with full coverage and ultralow surface RMS. The direct contact of fullerenes with PEDOT: PSS could be eliminated (See also Fig. S12). Accordingly, we ascribe the

Table 1

Reduction potential, LUMO level and HOMO level for C_{60} , BPB-M, PCBM, BPB-B, BPB-T and ICBA.

Fullerenes	E_1 (V) [#]	E_2 (V)	LUMO (eV) [†]	HOMO (eV) [‡]	E_g (eV)
C_{60}	-1.02	-1.46	-3.78	-5.63	1.85
BCB-M	-1.06	-1.47	-3.74	-5.59	1.85
PCBM	-1.12	-1.53	-3.68	-5.38	1.70
BPB-B	-1.19	-1.53	-3.61	-5.31	1.70
BPB-T	-1.32	-1.75	-3.48	-5.25	1.77
ICBA	-1.33	-1.79	-3.47	-5.24	1.77

[#] Reduction potentials $E_{\text{red } 1/2} = (E_{\text{ox } p} + E_{\text{red } p})/2$ were measured versus Ag/Ag^+ quasi-reference electrode as reference and were standardized to Fc/Fc^+ couple. E_1 and E_2 stand for the first and second half-wave reduction potentials, respectively.

[†] Calculated from the following equation: LUMO level = $-(E_{\text{red } 1/2} + 4.8)$ eV.

[‡] Calculated from the following equation: HOMO level = LUMO level - E_g . E_g is the optical band gap derived from absorption data [16,24].

variation of the performance to the use of different fullerene materials.

As reported by Huang *et al.*, the performance of nonexcitonic perovskite solar cells is independent of the LUMO energy level of the ETL materials and the high electron injection barrier [13]. Even

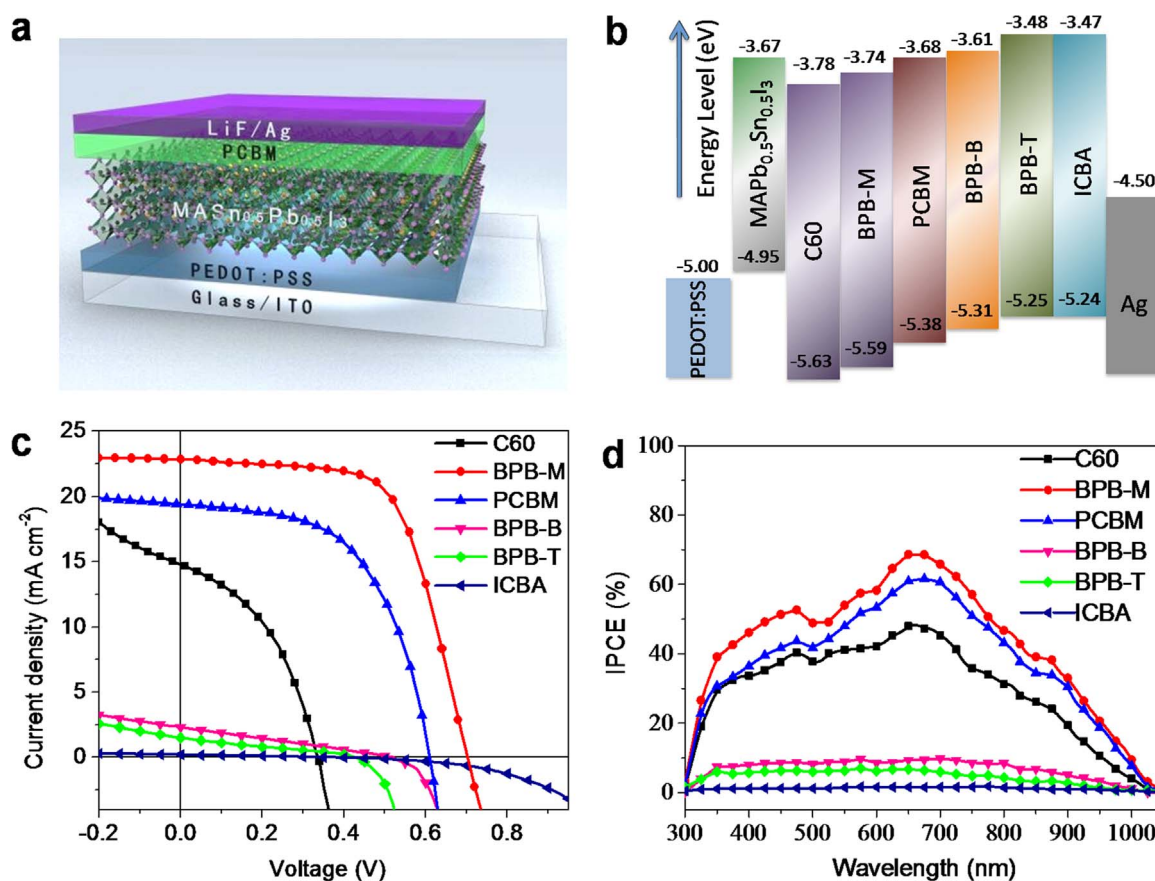


Fig. 2. Tin-lead organohalide perovskite and fullerene derivatives based PHJ solar cells. (a) Schematic of the $\text{MASn}_{0.5}\text{Pb}_{0.5}\text{I}_3$ /fullerene PHJ solar cell. (b) Energy diagram of various device layers. Here, HOMO level for $\text{MASn}_{0.5}\text{Pb}_{0.5}\text{I}_3$ was obtained from Ref. [11]. The energy levels were drawn relative to the vacuum level that is by definition set to zero. (c) J - V curves of $\text{MASn}_{0.5}\text{Pb}_{0.5}\text{I}_3$ perovskite PSCs under AM 1.5 simulated solar irradiation of 100 mW cm^{-2} with the scan-rate fixed at 50 mV s^{-1} . No stabilization time under light soaking and positive bias was applied before the measurements. (d) IPCE spectra of the $\text{MASn}_{0.5}\text{Pb}_{0.5}\text{I}_3$ perovskite PSCs.

though the LUMO energy levels of ETL materials are much higher than that of MAPbI_3 , the V_{OC} of MAPbI_3 perovskite solar cells is dominated by the perovskite layer itself, rather than the electron or hole collection layers. However, for $\text{MASn}_{0.5}\text{Pb}_{0.5}\text{I}_3$ based devices the ETL materials rather than the perovskite layer dominate the V_{OC} . This suggests that the exciton generation mechanism of TLOP solar cell device is different from the nonexcitonic MAPbI_3 photovoltaic device, but similar to excitonic semiconductor based devices such as organic polymer solar cells [27].

Exciton feature of semiconductor could be investigated by the marked changes in the photoluminescence (PL) spectra [28]. To further confirm the exciton feature of $\text{MASn}_{0.5}\text{Pb}_{0.5}\text{I}_3$ we characterized its PL spectra. However, in our experiments (See Fig. S13) and literature [29], the TLOP materials did not show PL response, which implies the exciton feature of $\text{MASn}_{0.5}\text{Pb}_{0.5}\text{I}_3$ might be different from LOP materials.

The dependence of EQE on illumination-intensity (I_{ill}) at low I_{ill} could give evidence for the exciton generation in photovoltaic device [30]. To further confirm the Frenkel exciton generation in these devices, we characterized the correlation of EQE and illumination-intensity at the wavelength of 650 nm in six kinds of $\text{MASn}_{0.5}\text{Pb}_{0.5}\text{I}_3$ / fullerene devices (See Fig. S14). In all the devices, the EQE slowly decreased as the increase of I_{ill} , which suggest the Frenkel exciton generation in the $\text{MASn}_{0.5}\text{Pb}_{0.5}\text{I}_3$ /fullerene solar cell [30].

Besides energy harvesting, detection of optical signals in the UV-Vis-NIR spectral region or panchromatic detection is critically important for a variety of applications including image sensing, remote control, environmental monitoring and night surveillance

[31]. High-performance infrared photodetectors (PDs) are currently dominated by inorganic semiconductor technologies, especially silicon-based devices. These devices are mostly fabricated on rigid substrates under strictly controlled fabrication conditions. Consequently, low-cost and high-performance infrared photodetectors are needed that can be fabricated by convenient techniques (e.g., printing or coating) at relatively low temperatures [32,33]. The solution processed $\text{MASn}_{0.5}\text{Pb}_{0.5}\text{I}_3$ /fullerenes PSCs we have fabricated can also work as photodetectors. Fig. 4a shows the photocurrent-intensity dependence of the PDs. It is worth mentioning here, when a weak light ($80 \mu\text{W cm}^{-2}$) switched ON/OFF, the devices still photoresponsive with ON/OFF ratio more than 10^2 (Fig. 4b). The intensity-dependent responsivity and detectivity of the $\text{CH}_3\text{NH}_3\text{Sn}_{0.5}\text{Pb}_{0.5}\text{I}_3$ /fullerene PSCs for incandescent light at zero bias is shown in Fig. S15. Due to the panchromatic absorption of the $\text{MASn}_{0.5}\text{Pb}_{0.5}\text{I}_3$, these devices have a broad response to monochromatic light in the spectral range between 300 and 1050 nm (Fig. 4c). For the perovskite heterojunction PDs with BPB-M as the ETL material, a detectivity of greater than 10^{12} Jones at 900 nm with zero bias applied was achieved (Fig. 4d). The fullerene-dependent photodetecting properties (ON/OFF ratio, Responsivity and Detectivity) further support the exciton dissociation feature in $\text{MASn}_{0.5}\text{Pb}_{0.5}\text{I}_3$ to be Frenkel exciton.

To further study the exciton dissociation behavior in $\text{MASn}_{0.5}\text{Pb}_{0.5}\text{I}_3$ perovskite material and to improve the PSC efficiency, we compared the photoresponse behavior of $\text{MASn}_{0.5}\text{Pb}_{0.5}\text{I}_3$ with conventional excitonic organic semiconductor in lateral architecture photosensors. Fig. 5a presents a schematic diagram of the TLOP/fullerene hybrid photosensor fabricated on a

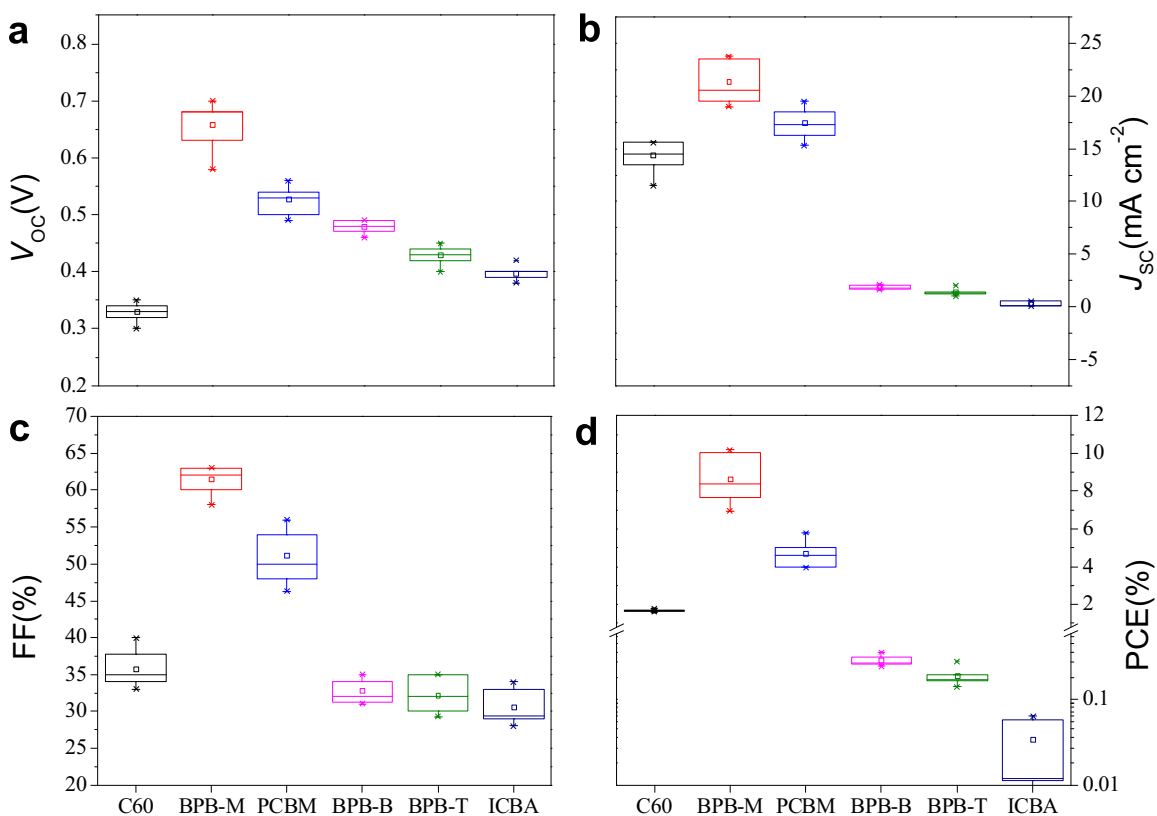


Fig. 3. Effect of electron transport materials on the photovoltaic performances of $\text{MASn}_{0.5}\text{Pb}_{0.5}\text{I}_3$ /fullerenes planar heterojunction solar cells. Histogram of the PSC photovoltaic parameters (a) V_{oc} , (b) J_{sc} , (c) FF, (d) PCE for more than 20 devices with the configuration ITO/PEDOT:PSS/Perovskite/Fullerene/LiF/Ag.

SiO_2/Si substrate. Au/Cr source/drain electrodes were deposited on the substrate by thermal evaporation through photolithography to form a channel with $6\ \mu\text{m}$ in length and $50\ \mu\text{m}$ in width (Fig. 5b). Fullerene or fullerene derivatives were spin-cast on the metal electrodes followed by spin-casting the TLOP layer (See details in Experimental). The energy levels of sandwich structure of the devices were shown in Fig. 5c. As shown in Fig. 5d, the device only based on pristine TLOP material without fullerene or fullerene derivatives exhibits extremely slow photoresponses at the bias of 100 mV. The current increased then decreased slowly when the light is switched ON/OFF, and no saturation could be observed. As the Fermi level of Au is lower than the HOMO energy level of TLOP material, we chose a higher Fermi level material (copper) as an electrode, and a similar phenomenon was observed, which excluded the influence of electrode material (Fig. S16). Nevertheless, as shown in Fig. 5e, the device based on TLOP material with a BPB-M interface layer shows much faster ON/OFF cycles of source-drain currents (I_{DS}) under the switch of light illumination. Similar results were obtained when other fullerene or fullerene derivatives were deposited as interface layer. In addition, even at a higher bias (1 V), the I - t curve showed the same phenomena as that at low bias (100 mV) (Fig. S17). Control experiments using only Au electrodes or fullerene/fullerene derivatives showed little photoresponse (Fig. S18). However, in the TLOP/BPB-M hybrid device, fullerene derivatives such as BPB-M showed the ability of assisting the separation of exciton. Photon absorption in the TLOP material generated electron-hole pairs, and the electrons in the conduct band of the perovskite were transferred to fullerene (or holes in the fullerene transferred to the perovskite) under the bias. The device based on poly(3-hexylthiophene-2,5-diyl) (P3HT), a commonly used polymer semiconductor with Frenkel excitonic feature, was also fabricated and characterized. The device based on P3HT showed slow photoresponse speed (Fig. 5f).

The light soaking effect, hysteresis effect, and ion migration of perovskite might affect the photoresponse of the film. To exclude the influence of these three features, the photoresponse of the control devices based on nonexcitonic MAPbI_3 and MASnI_3 were tested. Both of the devices showed highly fast photoresponse, which means that in vertical devices the photoresponse speed was almost not affected by these three features (See Fig. S19). Besides, as reported before, the light soaking effect, hysteresis effect and ion migration also do not obviously influence the photoresponse speed of perovskite materials [34–36]. Consequently, it could be confirmed that not light soaking effect, hysteresis effect, and ion migration of perovskite but the dissociation behavior cause the slow photoresponse speed of $\text{MASn}_{0.5}\text{Pb}_{0.5}\text{I}_3$ which is similar to that of P3HT suggesting the analogous excitonic feature of $\text{MASn}_{0.5}\text{Pb}_{0.5}\text{I}_3$ and P3HT.

Additionally, different fullerene or fullerene derivatives used in the lateral architecture photosensors also obviously influence the external quantum efficiency (EQE or photogain) revealing that the carriers collected on the electrodes are generated by a single-photon [37]. The EQE measured with the same perovskite and different fullerene or fullerene derivatives are shown in Fig. S18. The EQE results have showed a similar trend to that in vertical structure photovoltaic devices. The maximum EQE of the TLOP fullerene hybrid photosensors at the absorption wavelength of 1000 nm was about 200% with perovskite/BPB-M configuration (light intensity $I_{\text{ill}} = 1.01\ \text{mW/cm}^2$ and source-drain bias voltage $V_{DS} = 1\ \text{V}$). All of these hybrid photosensors are sensitive to NIR light with wavelengths from 800 to 1050 nm. The corresponding responsivity and detectivity are shown in Fig. S20, which are also obviously dependent on the fullerene materials used. These phenomena in planar photosensors further confirms that the exciton dissociation feature in $\text{MASn}_{0.5}\text{Pb}_{0.5}\text{I}_3$ likely is Frenkel exciton, and the exciton dissociation behavior is altered when the Sn: Pb ratio changes.

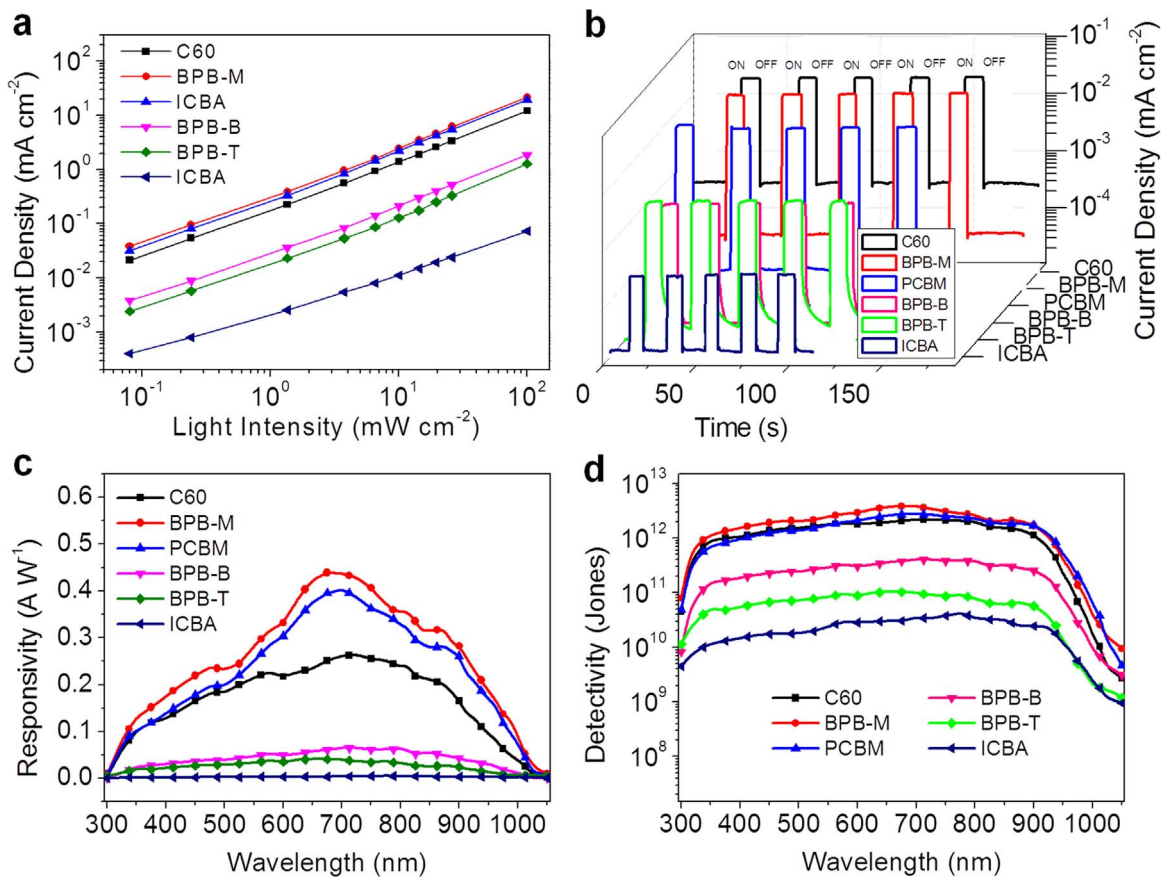


Fig. 4. Photoresponsive characterization of $\text{MASn}_{0.5}\text{Pb}_{0.5}\text{I}_3$ /fullerene PSCs. (a) Device photocurrents illuminated by incandescent light with different intensity at zero bias. (b) Photoresponses of the devices for weak light showing good cycling stability at zero bias, $I_{\text{th}} = 80 \mu\text{W cm}^{-2}$. (c) Wavelength-dependent responsivity and (d) detectivity of the devices at zero bias with light scanned from 300 to 1050 nm.

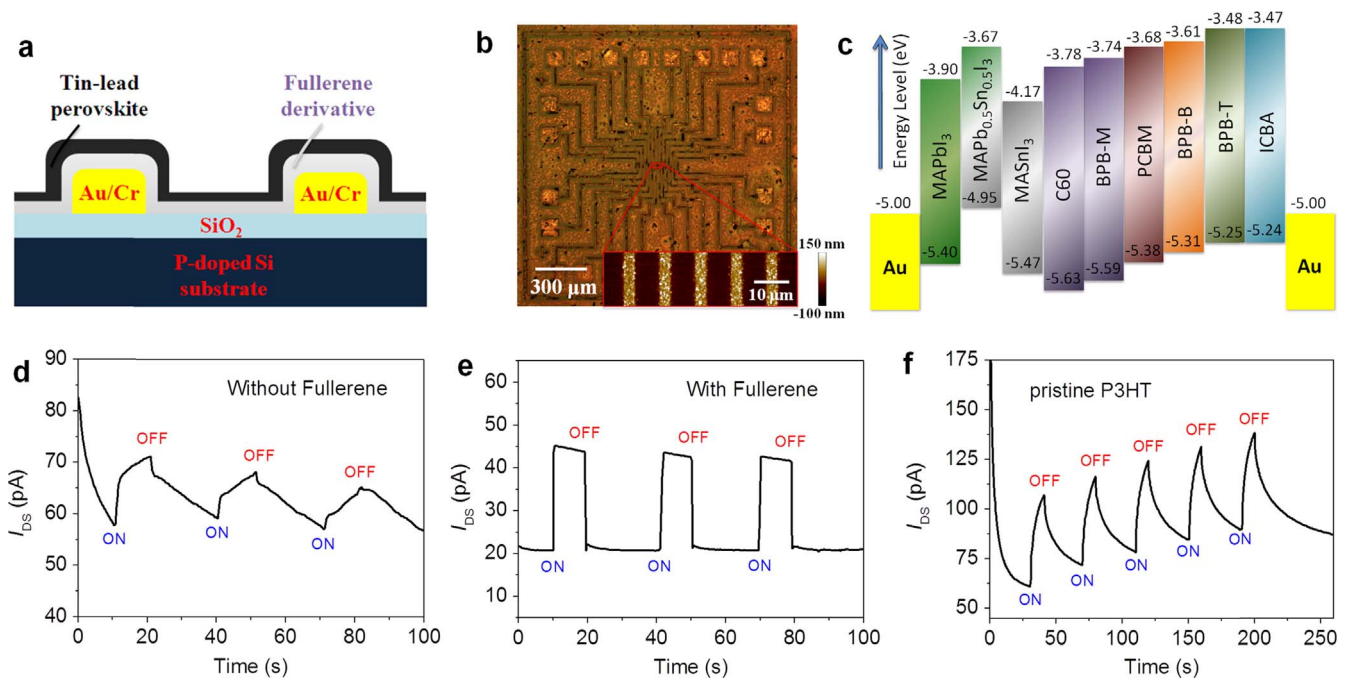


Fig. 5. Photoresponsive properties of $\text{MASn}_{0.5}\text{Pb}_{0.5}\text{I}_3$ and fullerene derivative based photosensors with the lateral architecture. (a) Schematic demonstration of a TLOP/fullerene based photosensor. (b) Optical micrograph of the photosensor arrayed with prepatterned gold electrodes on silicon wafer after spin-casting fullerene and perovskite material. Inset: AFM image of the central part. (c) Energy diagram of various materials in lateral photosensors. (d) The I - t curve of the $\text{CH}_3\text{NH}_3\text{Sn}_{0.5}\text{Pb}_{0.5}\text{I}_3$ device without fullerene stimulated by incandescent light with intensity 25.86 mW cm^{-2} , $V_{\text{DS}} = 100 \text{ mV}$. (e) The I - t curve of the $\text{CH}_3\text{NH}_3\text{Sn}_{0.5}\text{Pb}_{0.5}\text{I}_3$ device with BPB-M. (f) The I - t curve of the P3HT device without fullerene. The measure conditions in d, e and f are the same, including the substrate, bias, light intensity and testing environment.

To understand energy loss mechanisms in perovskite solar cells it is critical to investigate exciton generation, dissociation, and recombination processes. As these devices are based on the same light absorbing materials ($\text{MASn}_{0.5}\text{Pb}_{0.5}\text{I}_3$) and the same device architecture, the exciton generations must be analogous. Thus, we mainly ascribe the phenomena to the exciton dissociation or recombination. As shown in Fig. 4a, the devices exhibit nearly linear dependence of J_{SC} on various light intensities. It indicates that within this range, the photocurrent has a linear response as the incident light intensity varies, which means that exciton dissociation dominates the energy loss mechanism in the devices and the exciton recombination could be discounted [38]. From the IPCE result, the exciton dissociation efficiency in the devices based on C_{60} , BPB-M and BPB-B is much higher than those based on BPB-B, BPB-T and ICBA. That is to say, with optimized LUMO energy level of ETL materials, the exciton dissociation efficiency of ($\text{MASn}_{0.5}\text{Pb}_{0.5}\text{I}_3$) could be improved which is coincide with Frenkel donors.

Thus, the enhanced IPCE of the device proves the exciton feature of $\text{MASn}_{0.5}\text{Pb}_{0.5}\text{I}_3$ is Frenkel exciton which indicates that $\text{MASn}_{0.5}\text{Pb}_{0.5}\text{I}_3$ photovoltaic solar cells should be treated as traditional organic thin film photovoltaic devices, rather than inorganic ones.

However, as could be seen in the Fig. S12, even though the thickness of $\text{MASn}_{0.5}\text{Pb}_{0.5}\text{I}_3$ is about 280 nm to 320 nm in the photovoltaic device, the photo-generated exciton could still diffuse from the inside of the TLOP material to the ETL/HTL and dissociate into free charge (hole or electron). This means that this material could work in the planar heterojunction architecture with high performance like MAPbI_3 . On the other hand, the reported exciton binding energy of $\text{MASn}_{0.5}\text{Pb}_{0.5}\text{I}_3$ is much lower than that of traditional organic semiconductor and also lower than the thermal energy such that it allow the generation of Wannier-Mott exciton at room temperature [23]. These facts suggests the exciton feature of $\text{MASn}_{0.5}\text{Pb}_{0.5}\text{I}_3$ is Wannier-Mott exciton, which implies that $\text{MASn}_{0.5}\text{Pb}_{0.5}\text{I}_3$ photovoltaic solar cells should be treated as traditional inorganic thin film photovoltaic devices, rather than organic ones. Based on both aspects mentioned above, we assign the exciton feature of $\text{MASn}_{0.5}\text{Pb}_{0.5}\text{I}_3$ to Frenkel-Wannier-Mott hybridization. It is the first time to report that this perovskite material has Frenkel and Wannier-Mott exciton features simultaneously.

3. Conclusions

In summary, by optimizing the preparation of the perovskite layer and carefully selecting the ETL materials, high performance $\text{MASn}_{0.5}\text{Pb}_{0.5}\text{I}_3$ solar cells were constructed with light harvesting up to 1050 nm. The performance of TLOP perovskite PHJ solar cells was rather sensitive to the variation of the LUMO level of ETL materials, and the highest PCE could be over 10% with high J_{SC} of 22.8 mA cm^{-2} . This suggests that $\text{MASn}_{0.5}\text{Pb}_{0.5}\text{I}_3$ perovskite is excitonic semiconductor with Frenkel-Wannier-Mott exciton hybridization feature, which is valuable to the achievement of high performance and low pollution tin-lead organohalide perovskite solar cells through low temperature solution process. Benefiting from the panchromatic absorption of TLOP, high performance PDs with broad response spectral range from UV-Vis to NIR have been achieved in both vertical and lateral architectures. Our results will motivate the pursuit of high performance optoelectronic devices with low environmental pollution.

4. Experimental

4.1. Perovskites precursor synthesis

$\text{CH}_3\text{NH}_3\text{I}$ (MAI) was synthesized by neutralizing equimolar amounts of HI and CH_3NH_2 . PbI_2 and SnI_2 (purchased from Aldrich without further purification) were dissolved with MAI (1:1:2, 0.75:1.25:2 and 0.5:1.5:2 by mole, respectively) into dimethyl sulfoxide (DMSO): g-butyrolactone (GBL) (3:7, v/v) solvent in a nitrogen-filled glove box with oxygen and moisture levels < 1 ppm. The mixed solution was then heated at 65°C for about 0.5 h to make sure it was fully dissolved.

4.2. Fullerene materials synthesis

The detail is described in [Supplementary material](#).

4.3. Perovskite materials characterization

The perovskite precursor solution was spin-cast (5000 r/min for 30 s) onto silicon wafer (300 nm SiO_2 on p-doped Si substrate) with hydrophilic pre-treatment by reactive ion etching (RIE) or ITO/PEDOT: PSS substrate for $\text{MASn}_{0.5}\text{Pb}_{0.5}\text{I}_3$ characterization. The X-ray diffraction spectrum of the perovskite material prepared in this work was collected on a Bruker D8-Advance X-ray powder diffractometer with $\text{Cu K}\alpha$ radiation ($\lambda = 1.5406 \text{ \AA}$, step size 0.02°). The absorption spectroscopy was carried out by Agilent Cary 5000 UV-Visible spectrometer. SEM and EDX characterization were performed on a Hitachi S4800. AFM image was taken with tapping mode on a Bruker Dimension EDGE.

4.4. Fullerene materials characterization

The cyclic voltammogram measurements were performed through a CHI660D electrochemical analyzer with tetrabutylammonium perchlorate (TBAClO_4 , 0.10 M) in o-DCB/acetonitrile (4:1) mixtures as the electrolyte and ferrocene as internal standard at a scan rate of 100 mV s^{-1} . The working electrode, counter electrode and quasireference electrode are glassy-carbon, platinum wire and Ag wire, respectively. The UV-Visible characterization was carried out through an Agilent Cary 5000 spectrometer (10^{-5} M in toluene). ^1H and ^{13}C NMR spectra were conducted on a 500 MHz Bruker AVANCE III and referenced to the solvent peak. MALDI-TOF mass spectra were recorded on a Bruker Autoflex with alphacyanocinnamic Acid (CCA) as matrix. FTIR spectra were obtained on a Thermal Fisher Nicolet iN10 spectrometer.

4.5. Solar cells fabrication

ITO glasses ($15 \Omega \text{ sq}^{-1}$, purchased from Zhuhai Kaivo Co. Ltd) were ultrasonically cleaned in detergent, distilled water, acetone, and isopropanol for 15 min, respectively. The cleaned ITO glasses were dried with high-pressure nitrogen gas and then on hot plate at 120°C for 20 min. The PEDOT: PSS was spin-cast (4000 r/min for 60 s) on the cleaned ITO substrate after it was exposed to UV-ozone for 30 min. The fully dissolved tin-lead iodide and MAI mixed solution (1:1:2 by mole) was spin-cast (5000 r/min for 30 s) onto the PEDOT: PSS layer followed by spin-casting a drop of toluene at 5000 r/min for 4 s in glove box. These films were then thermally annealed at 100°C for 10 min and cooled to room temperature. The fullerene/fullerene derivatives were dissolved in chlorobenzene (CB) with a concentration of 15 mg/ml and then spin-cast (1000 r/min for 30 s) onto the $\text{MASn}_{0.5}\text{Pb}_{0.5}\text{I}_3$ film in glove box. After solvent annealing in glass Petri dishes, a thickness of 0.5 nm LiF and 100 nm silver top electrodes were deposited on

the active layer under a vacuum of 3×10^{-4} Pa in a thermal evaporator. The device area, as defined by the anode-cathode overlap, was 0.06 cm^2 .

4.6. Solar cells characterization

The electrical measurement was conducted in Keithley 4200 source measure unit. All the samples were measured at room temperature and in air with humidity lower than 50%. Solar cells were measured with masked area $1 \text{ mm} \times 1 \text{ mm}$. The light illumination (100 mW cm^{-2} AM 1.5 G) was provided with a San-Electric XES-70S1 solar simulator, and the light intensity was calibrated through a photovoltaic reference cell with certification of the PV lab of Technology and Application Center (Newport calibration cert. #0885).

4.7. Lateral devices fabrication

The fully dissolved tin-lead iodide and MAI mixed solution (1:1:2 by mole) was spin-cast (5000 r/min for 30 s) onto the fullerene covered/uncovered silicon wafer (300 nm SiO_2 on p-doped Si substrate) with 8 nm Cr/60 nm Au (or Cu) pre-deposited through photolithographically-patterned photoresist masks. Then, a drop of toluene was spin-cast onto the top of the perovskite film at 5000 r/min for 4 s. This pristine film was thermally annealed at 100°C for 10 min and cooled to room temperature.

4.8. Lateral devices characterization

Optical and SEM images were taken by Nikon Eclipse LV100 and Hitachi S4800 with an acceleration voltage of 5 kV. The photoconductive measurement was conducted using a Karl Suss PM5 probe station equipped with an Agilent 4155C semiconductor parameter analyzer. A 150 W Halogen lamp and a 150 W Xe lamp (TLS1509–150A, Beijing Zolix Instruments Co., Ltd) provided the sources of the incandescent and monochromatic light for illumination, respectively, with power intensity measured by a LPE-1A laser power energy meter (Beijing Phycience Opto-Electronics Co., Ltd). All the samples were measured in air with humidity lower than 50% at room temperature.

Acknowledgments

We thank the National Natural Science Funds of China (21271174, 21225311, 91333102, 21402202, 21373014 and 51121091) and the 973 Project (2012CB932601 and 2012CB921404) for financial support.

Appendix A. Supplementary material

Supplementary data associated with this article can be found in the online version at <http://dx.doi.org/10.1016/j.nanoen.2016.08.015>.

References

- [1] D.Y. Liu, T.L. Kelly, *Nat. Photon.* 8 (2014) 133–138.
- [2] F. Hao, C.C. Stoumpos, D.H. Cao, R.P.H. Chang, M.G. Kanatzidis, *Nat. Photon.* 8 (2014) 489–494.
- [3] M.A. Green, A. Ho-Baillie, H.J. Snaith, *Nat. Photon.* 8 (2014) 506–514.
- [4] Q. Shen, Y. Ogomi, J. Chang, S. Tsukamoto, K. Kukiwara, T. Oshima, N. Osada, K. Yoshino, K. Katayama, T. Toyoda, S. Hayase, *Phys. Chem. Chem. Phys.* 16 (2014) 19984–19992.
- [5] G.E. Eperon, S.D. Stranks, C. Menelaou, M.B. Johnston, L.M. Herz, H.J. Snaith, *Energy Environ. Sci.* 7 (2014) 982–988.
- [6] S. Sun, T. Salim, N. Mathews, M. Duchamp, C. Boothroyd, G. Xing, T.C. Sum, Y. M. Lam, *Energy Environ. Sci.* 7 (2014) 399–407.
- [7] Y. Ogomi, A. Morita, S. Tsukamoto, T. Saitho, Q. Shen, T. Toyoda, K. Yoshino, S. S. Pandey, T. Ma, S. Hayase, *J. Phys. Chem. C* 118 (2014) 16651–16659.
- [8] G.E. Eperon, V.M. Burlakov, A. Goriely, H.J. Snaith, *ACS Nano* 8 (2014) 591–598.
- [9] L. Zuo, Z. Gu, T. Ye, W. Fu, G. Wu, H. Li, H. Chen, *J. Am. Chem. Soc.* 137 (2015) 2674–2679.
- [10] F. Hao, C.C. Stoumpos, R.P.H. Chang, M.G. Kanatzidis, *J. Am. Chem. Soc.* 136 (2014) 8094–8099.
- [11] Y. Ogomi, A. Morita, S. Tsukamoto, T. Saitho, N. Fujikawa, Q. Shen, T. Toyoda, K. Yoshino, S.S. Pandey, T.L. Ma, S. Hayase, *J. Phys. Chem. Lett.* 5 (2014) 1004–1011.
- [12] H.J. Feng, T.R. Paudel, E.Y. Tsymal, X.C. Zeng, *J. Am. Chem. Soc.* 137 (2015) 8227–8236.
- [13] M. Hu, C. Bi, Y. Yuan, Z. Xiao, Q. Dong, Y. Shao, J. Huang, *Small* 11 (2015) 2164–2169.
- [14] Y.Y. Lai, Y.J. Cheng, C.S. Hsu, *Energy Environ. Sci.* 7 (2014) 1866–1883.
- [15] A. Mohajeri, A. Omidvar, *Phys. Chem. Chem. Phys.* 17 (2015) 22367–22376.
- [16] G. Lin, R. Cui, H. Huang, X. Guo, S. Yang, C. Li, J. Dong, B. Sun, *Tetrahedron* 71 (2015) 7998–8002.
- [17] L. Hu, R. Cui, H. Huang, G. Lin, X. Guo, S. Yang, Y. Lian, J. Dong, B. Sun, *J. Nanosci. Nanotechnol.* 15 (2015) 5285–5290.
- [18] K. Vandewal, Z.F. Ma, J. Bergqvist, Z. Tang, E.G. Wang, P. Henriksson, K. Tvingstedt, M.R. Andersson, F.L. Zhang, O. Inganäs, *Adv. Funct. Mater.* 22 (2012) 3480–3490.
- [19] D. Di Nuzzo, G. Wetzelaer, R.K.M. Bouwer, V.S. Gevaerts, S.C.J. Meskers, J. C. Hummelen, P.W.M. Blom, R.A.J. Janssen, *Adv. Energy Mater.* 3 (2013) 85–94.
- [20] T.L. Andrew, V. Bulovic, *ACS Nano* 6 (2012) 4671–4677.
- [21] K. Sun, J. Chang, F.H. Isikgor, P. Li, J. Ouyang, *Nanoscale* 7 (2015) 896–900.
- [22] J. Seo, S. Park, Y.C. Kim, N.J. Jeon, J.H. Noh, S.C. Yoon, S.I. Sang, *Energy Environ. Sci.* 7 (2014) 2642–2646.
- [23] Q. Shen, Y. Ogomi, J. Chang, T. Toyoda, K. Fujiwara, K. Yoshino, K. Sato, K. Yamazaki, M. Akimoto, Y. Kuga, K. Katayama, S. Hayase, *J. Mater. Chem. A* 3 (2015) 9308–9316.
- [24] F.B. Kooistra, J. Knol, F. Kastenberger, L.M. Popescu, W.J.H. Verhees, J.M. Kroon, J. C. Hummelen, *Org. Lett.* 9 (2007) 551–554.
- [25] H. Zhang, H. Azimi, Y. Hou, T. Ameri, T. Przybilla, E. Spiecker, M. Kraft, U. Scherf, C.J. Brabec, *Chem. Mater.* 26 (2014) 5190–5193.
- [26] Q. Wang, Y.C. Shao, Q.F. Dong, Z.G. Xiao, Y.B. Yuan, J.S. Huang, *Energy Environ. Sci.* 7 (2014) 2359–2365.
- [27] G.D. Han, W.R. Collins, T.L. Andrew, V. Bulovic, T.M. Swager, *Adv. Funct. Mater.* 23 (2013) 3061–3069.
- [28] J.J. Piet, P.N. Taylor, B.R. Wgweij, H.L. Anderson, A. Osuka, J.M. Warman, *J. Phys. Chem. B* 105 (2001) 97–104.
- [29] C.C. Stoumpos, C.D. Malliakas, M.G. Kanatzidis, *Inorg. Chem.* 52 (2013) 9019–9038.
- [30] A.J. Moule, K. Meerholz, *Appl. Phys. B* 92 (2008) 209–218.
- [31] F.-C. Chen, S.-C. Chien, G.-L. Ciou, *Appl. Phys. Lett.* 97 (2010) 103301.
- [32] S.-T. Chuang, S.-C. Chien, F.-C. Chen, *Appl. Phys. Lett.* 100 (2012) 013309.
- [33] R. Dong, C. Bi, Q. Dong, F. Guo, Y. Yuan, Y. Fang, Z. Xiao, J. Huang, *Adv. Opt. Mater.* 2 (2014) 549–554.
- [34] G. Lin, Y. Lin, R. Cui, H. Huang, X. Guo, J. Dong, X. Guo, B. Sun, *J. Mater. Chem. C* 3 (2015) 10793–10798.
- [35] J.H. Heo, M.S. You, M.H. Chang, W. Yin, T.K. Ahn, S. Lee, S. Sung, D., H. Kim, S. H. Im, *Nano Energy* 15 (2015) 530–539.
- [36] Z. Xiao, Y. Yuan, Y. Shao, Q. Wang, Q. Dong, C. Bi, P. Sharma, A. Gruverman, J. Huang, *Nat. Mater.* 14 (2014) 193–198.
- [37] Y. Lin, X. Guo, *Small* 11 (2015) 2856–2861.
- [38] M. Stollerfoht, B. Philippa, S. Shoaee, H. Jin, W. Jiang, R.D. White, P.L. Burn, P. Meredith, A. Pivrikas, *J. Phys. Chem. C* 119 (2015) 26866–26874.



Dr Guoming Lin obtained his Ph.D. in Institute of High Energy Physics, Chinese Academy of Sciences. He is currently a research assistant in Fujian Institute of Research on the Structure of Matter. His research focuses on novel organic-inorganic hybrid nanomaterials and optoelectronic devices.



Yuanwei Lin was born in 1989 and is currently an engineer of North Microelectronics Corporation in China. He received his B.S. from Beijing Institute of Technology in 2011 and obtained his from Peking University in 2016. His research interests include carbon nanomaterial based devices and optoelectronic materials/devices.



Jinquan Dong got his master degree in Perking University in 1987. He is currently a senior engineer of Institute of High Energy Physics, Chinese Academy of Sciences. His research interest is the synthesis of Fullerenols and metallofullerenols.



Huan Huang obtained her pH. D. from Peking University, China, working in the preparation and study of fullerene derivatives under the supervision of Prof. L. B. Gan. After that, she joined the group of Prof. B. Y. Sun in Institute of High Energy Physics, Chinese Academy of Sciences, as a research assistant. Her current research interests include the preparation and study of multi-component, fullerene-based donor-acceptor molecular materials.



Dr. Xuefeng Guo received his pH. D. in 2004 from the Institute of Chemistry, Chinese Academy of Sciences, Beijing. From 2004 to 2007, he was a postdoctoral research scientist at the Columbia University Nanocenter. He joined the faculty as a professor under "Peking 100-Talent" Program at Peking University in 2008. In 2012, he won the National Science Funds for Distinguished Young Scholars of China. He has over 120 scientific papers, including *Science*, *Nature Nanotech.*, *Chem. Rev.*, *Acc. Chem. Res.* and *Chem. Soc. Rev.* et al.. His current research is focused on nanometer/molecular electronics, organic/flexible electronics and single-molecule detection.



Dr. Rongli Cui received her pH. D. in Inorganic Chemistry from University of Peking. She is now a research assistant at Carbon Nanomaterials Laboratory of Institute of High Energy Physics, Chinese Academy of Sciences. Her research focuses on the synthesis, properties and applications of novel structure carbon nanomaterials.



Baoyun Sun is a professor at the CAS Key Laboratory for Biomedical Effects of Nanomaterials and Nanosafety, Institute of High Energy Physics of CAS, and the National Center for Nanoscience and Technology of China. She got her pH. D. degree at Peking University and then worked at Department of Chemistry, Nagoya University, as a postdoctoral fellow (JSPS) and a researcher (JST). Then she moved to Leibniz Institute for Solid State and Materials Research, Germany, to continue her research. From 2006, she has worked at CAS as a Hundred Elite Professor. Prof. Sun's research interest is in chemistry and physics of fullerenes, nanotubes, and other carbon-based materials. She has published more than 60 papers. 23 patents had been licensed. She invented and built the first pilot-scale production line of metallofullerenes in the world.

23 patents had been licensed. She invented and built the first pilot-scale production line of metallofullerenes in the world.



Dr. Xihong Guo is currently an associate professor in Institute of High Energy Physics, Chinese Academy of Sciences. She received her pH. D. degree from Beijing Normal University. Her research interest is mainly on application of functional carbon nanomaterials, electrochemical sensors and fuel cells.



Bing Liu is a master student at the Institute of High Energy Physics Chinese Academy of Sciences. She received her Bachelor of Engineering in Pharmaceutical Engineering from Beijing Institute of Technology in 2014. Her research interests include organic and perovskite solar cells.